The control of thin film morphology by the interplay of dewetting, phase separation and microphase separation

2005 J. Phys.: Condens. Matter 17 S363

(http://iopscience.iop.org/0953-8984/17/9/006)

INSTITUTE OF PHYSICS PUBLISHING JOURNAL OF PHYSICS: CONDENSED MATTER

J. Phys.: Condens. Matter **17** (2005) S363–S386 doi:10.1088/0953-8984/17/9/006

The control of thin film morphology by the interplay of dewetting, phase separation and microphase separation

P Müller-Buschbaum[1,3], E Bauer[1], O Wunnicke[2,4] and M Stamm[2]

[1] TU München, Physik-Department, LS E13, James-Franck-Straße 1, 85748 Garching, Germany
[2] Leibniz Institut für Polymerforschung, Hohe Straße 6, 01069 Dresden, Germany

E-mail: muellerb@ph.tum.de

Received 24 November 2004
Published 18 February 2005
Online at stacks.iop.org/JPhysCM/17/S363

Abstract

In thin film geometry, the interplay between dewetting and phase separation or microphase separation controls the morphology of the polymeric structures resulting on a solid support. For the model system of polystyrene, polyparamethylstyrene and the diblock copolymer of the two homopolymers, the regime of ultrathin films is addressed experimentally. Evolving structures are probed with real and reciprocal space analysis techniques such as the optical microscopy, phase measuring interference microscopy, scanning force microscopy, neutron or x-ray reflectivity and grazing incidence small angle neutron or x-ray scattering approaches. The effective interface potential of the solid support is tuned by means of a change of the silicon substrate coating. Coating layers of silicon oxide, polyamide and polyimide are under investigation. A power law behaviour describing the most prominent in-plane length as a function of the initially prepared film thickness is observed. All reported structures have been prepared on large scale surfaces, such as typical Si wafers with 100 mm diameter.

(Some figures in this article are in colour only in the electronic version)

1. Introduction

Patterning of surfaces finds numerous applications in printing technologies, electronic chip production, fabrication of bioanalytical assays, sensors, coatings and other areas. In general, two main routes for preparation of surface patterns can be identified: lithography [1] and self-assembly (or minimization of free energy densities) [2]. In both, control of the resulting structures is gained by different approaches.

[3] Author to whom any correspondence should be addressed.
[4] Present address: Infineon Technologies, Koenigsbruecker Straße 180, 01099 Dresden, Germany.

In traditional lithography, a photoresist film is deposited on a solid support and irradiated (UV, x-ray, plasma etc) through a photomask. It is mainly polymer layers that are used as sacrificial layers and they are removed via a wet chemistry step [3]. Alternative approaches rely on photoinduced chemical reactions of functional groups of the photoresist and the irradiated polymer must not be removed [4]. Following the approach of soft lithography, structures down to several tens of nm are accessible [5]. Most likely lithography techniques comparable to the common resist technique in the semiconductor industry are used for the creation of anisotropic surface patterns. The anisotropy of the resulting structures requires a high orientation as well as position control of the patterned surface for further preparation steps.

One way to prepare patterns which are isotropic on a large scale is based on self-assembly or minimization of free energy densities [6–9]. Pattern isotropy offers the advantage of universal surface features which are not orientation dependent. Thus typical applications are in producing sensors, coatings and electronic devices for special optical applications (such as in light emitting diodes). Self-assembly and minimization of free energy densities are basically driven by different distinct processes [10, 11]. While surface structures resulting from phase separation in polymer blend films are typically of micrometre size, microphase separation in diblock copolymer systems is well known to offer nanostructures in the bulk as well as in thin films [12]. In the thin film geometry the interaction with the underlying substrate material adds dewetting as a further structure directing mechanism [13]. The interplay between dewetting and phase separation [14, 15] as well as dewetting and microphase separation [16, 17] enriches the 'zoo' of accessible structures, without increasing complexity via the addition of a third or fourth polymeric component. To access the regime of nanopatterned films a drastic decrease of the polymer film thickness is necessary.

Within this paper we focus on possible routes of preparation of nanopatterns following these ideas. Thus we restrict consideration to the regime of confined thin films with initial film thickness smaller than twice the radius of gyration of the unperturbed molecule. Films are prepared by spin coating to access this regime [18]. Confined homopolymer films, polymer blend films as well as diblock copolymer films are subjected to destabilization via solvent vapour storage. As a consequence, the thin film morphology results from an interplay between dewetting, phase separation and microphase separation. Solvent vapour storage has been developed as an alternative to annealing above the glass transition of the polymers [19]. After the initial preparation of the polymer film, exposure to a solvent vapour lowers the glass transition temperature. The polymer layer is swollen by the solvent (e.g. toluene) molecules incorporated from the surrounding atmosphere, which act as a plasticizer. As a consequence of the different solubilities of various polymers in the solvent used, the swellings differ for the two polymers in a binary blend or the two blocks of a block copolymer. The original homogeneous polymer film is replaced by a highly concentrated polymer–solvent solution layer. Therefore the viscosity and surface tension are reduced. In addition, the long range interaction changes. The polymer–substrate van der Waals interaction is replaced by a polymer/solvent–substrate interaction. This changes the effective Hamaker constant of the system. By extracting the solvent (e.g. toluene) molecules in a solvent quench, the polymeric structure build-up produced by the remaining homopolymers or diblock copolymers is frozen in and stabilized.

As compared to the outcome of the original spin coating process, the surface patterns obtained are different. In spin coating, a polymer solution at low concentration is placed on the substrate and subjected to rotation. In a simple model, the spin coating is understood as a three-step process [18]: during the initial stages, called phase one, most of the solution is centrifuged off, leaving a thin solution layer on the substrate; as the layer thins due to fluid flow (phase two), the evaporation of the solvent becomes important—the evaporation increases the

viscosity of the polymer solution and slows the shear thinning of the film; in the third phase, solvent evaporation causes the developing surface structure to freeze in. Generally, structures are created in a non-equilibrium stage, as demonstrated in many investigations (see [20] and references therein). The non-equilibrium condition results from the rapid solvent quench, since typical spin coating times are of the order of only 30 s. In contrast, typical solvent storage times used within the investigation presented are longer than 6 h and adapted for accessing equilibrium conditions. Equilibrium is defined as the stability of the resulting structure with respect to a longer solvent vapour storage time and is experimentally investigated in kinetic experiments [21, 22].

Typically, structures have been prepared on large scale surfaces, such as Si wafers with 100 mm diameter. Control of the thin film morphology emerges from the determination of the power law dependences between spatial correlations and the initially prepared film thickness. As a consequence, the size and the spatial arrangement of the polymeric domains becomes predictable for future applications.

The paper is structured as follows. The introduction is followed by two experimental sections describing the experimental techniques used and the sample preparation applied. In the three subsequent sections the structures observed in homopolymer, polymer blend and diblock copolymer films are presented and discussed. A summary and an outlook finish the paper.

2. Experimental techniques

Due to the complexity of the evolving surface structures a combined real and reciprocal space analysis was performed. Real space techniques are imaging techniques yielding a direct indication of the surface structure. With increasing in-plane resolution, data were recorded by optical microscopy (OM), phase measuring interference microscopy (PMIM) and scanning force microscopy (SFM). From scattering experiments, information in reciprocal space resulted. Because in thin film geometry naturally polymeric material on a solid support is under investigation, in the scattering experiments a reflection geometry was used. By means of the probes applied, neutrons or x-rays (synchrotron radiation), the scattering length density contrast in the system was tailored. From reflectivity data, neutron reflectivity (NR) or x-ray reflectivity (XR), the density profile perpendicular to the substrate surface was obtained. With grazing incidence small angle neutron scattering (GISANS) as well as with grazing incidence small angle x-ray scattering (GISAXS), lateral structures were addressed, with high statistical significance, on the film surface as well as ones buried inside the film.

2.1. Optical microscopy (OM)

Optical microscopy (OM) is used to study the sample surface morphology on an in-plane length scale of several micrometres. Images were obtained with the ZEISS Axiotech 25H optical microscope with magnifications between 4 and 100 times (recorded by a HITACHI KP-D50 CCD camera). Due to the difference in the reflectivities for optical light, the solid supports and the polymeric material can be distinguished. The resulting pictures exhibit different greyscale values. For a statistical analysis of the optical micrographs the images were 2D Fourier transformed [23]. To calculate the power spectral density function (PSD), the 2D Fourier transforms were radially averaged next. From the PSD, dominant lateral length scales are extractable. A direct comparison with scattering data is not possible because instead of height data (as yielded e.g. from SFM) only greyscale data are subjected to Fourier transformation.

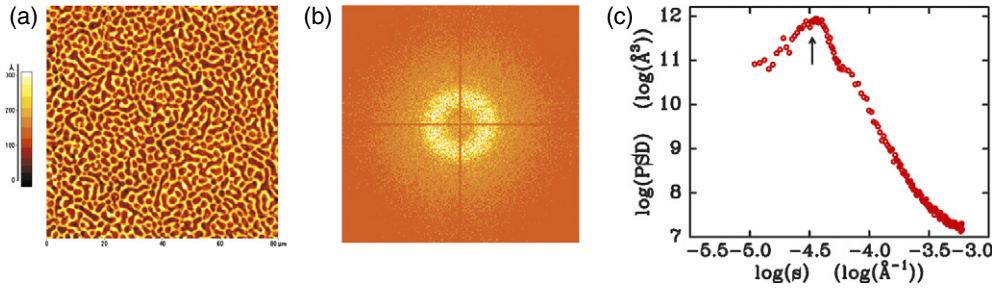

Figure 1. Statistical analysis of SFM data. (a) An example of topography data measured in non-contact mode in a scan range of 80 μm $\times$ 80 μm, picturing the surface of a binary polymer blend film [26]. This kind of surface structure is typical for a phase separation process. (b) A calculated two-dimensional Fourier transform displaying a ring of intensity in the Fourier space—a signature of an isotropic structure. (c) After radial averaging, a power spectral density (PSD) function results. The PSD functions for different scan ranges can be combined into one master curve. In the double-logarithmic presentation, the master curve is shown as a function of the inverse length s.

2.2. Phase measuring interference microscopy (PMIM)

For an optical characterization of the samples with a lateral resolution of approximately 1 μm and a height resolution better than 1 nm, a LOT/ZYGO phase measurement interference microscope was used. The interference pattern of monochromatic light reflected from a flat reference surface and the sample investigated is recorded in an area detector while the reference plane is moved with a piezoelectric device [24]. A magnification of 100 times was used. The area for which a data analysis had been performed was 42.2 μm $\times$ 42.2 μm.

2.3. Scanning force microscopy (SFM)

To resolve length scales smaller than 1 μm scanning force microscopy (SFM) was used [25]. Experiments in non-contact mode were performed with an Autoprobe CP atomic force microscope and in tapping mode with a Digital Instrument DI3100 microscope. Especially for the ultrathin films, non-contact mode experiments were necessary in order to minimize tip-induced sample degradation. From the tapping mode studies, phase contrast analysis enabled information about the surface mechanics to be obtained, in addition to the pure topography data. The image acquisition was done in air at room temperature and several images at different positions were measured for each sample. The scan range was adapted to the feature size of the polymeric structures. For very high resolution SFM imaging, we used gold coated silicon cantilevers with tips featuring a high aspect ratio and an asymptotic conical shape. The typical radius of curvature (10 nm) of the tips is small as compared to the surface structures measured (larger than 100 nm). Figure 1(a) shows an example of a surface topography as measured with SFM in non-contact mode.

Using the SFM software, a root mean square (rms) surface roughness is calculated from the three-dimensional topography data. This rms roughness displays the deviation of the individual heights from the mean surface and statistically describes the sample perpendicular to the surface [27]. Its value can be readily compared with the rms roughness resulting from reflectivity measurements.

To determine a statistical description parallel to the sample surface, the power spectral density (PSD) function needs to be calculated [28]. From a two-dimensional Fourier transformation an intensity distribution in reciprocal space is obtained, as shown in figure 1(b). In the case where a ring of intensity appears (as demonstrated for the particular example chosen

here), after a radial averaging the PSD results. Repeating these steps with SFM data collected for different scan ranges yields a set of PSD functions covering different ranges in reciprocal space (dictated by the resolution and the maximal scan range of the individual SFM data). To enlarge the total accessible range in reciprocal space, in a final step these PSD functions are merged into one (so-called) master curve [29, 14], as shown in figure 1(c). The position $s^\star$ of the intensity peak (shown by the arrow in figure 1(c)) corresponds to the most prominent in-plane length $\xi = 2\pi/s^\star$ statistically describing the surface structure parallel to the sample surface.

2.4. X-ray reflectivity (XR)

The x-ray reflectivity measurements were performed at the A2 polymer beamline of the DORIS III storage ring at HASYLAB (DESY, Hamburg) at a wavelength $\lambda = 0.15$ nm. The sample was placed horizontally and mounted inside a special reflectivity chamber. This enables the collection of reflectivity data *in situ* during annealing. Model fits to the data were calculated using a matrix formalism [30]. The interfaces were described by a hyperbolic tangent refractive index profile with the interfacial rms roughness σ. This profile is commonly used for silicon substrates [31] as well as for the interface between polymers [32]. In the case of polymer interfaces it is based on the volume fraction profile ϕ of one component, which can be described by a tanh profile to a good approximation [33]. Deviations originating from the concentration dependence of χ or the limited validity of the approximations used in the calculation of ϕ [34] are neglected. The interface profile of a dewetted layer was parametrized according to the results of the analysis of the atomic force microscopy and optical phase interference microscopy data and not varied in the fit. In the x-ray reflectivity measurements the density profile is laterally averaged over the illuminated sample area. Therefore holes in the film cause a reduction of the apparent scattering density of the material.

2.5. Neutron reflectivity (NR)

Specular scattering experiments yielding neutron reflectivity data were performed at the D17 beamline (ILL, Grenoble) in the time-of-flight mode using a wavelength band of $\lambda = 0.22$–2.20 nm. Typically one or two fixed angles of incidence were chosen and the resolution was adapted to the thickness of the sample under investigation. For further details concerning the beamline, see [35, 36]. Since in the refractive index in the case of synchrotron radiation the electron dispersion is replaced by the neutron scattering length density, the contrast can be changed by deuteration of the polymeric components. Model fits were calculated following the above-explained ideas.

2.6. Grazing incidence small angle x-ray scattering (GISAXS)

The use of a grazing incidence geometry enhances the surface sensitivity. Grazing incidence small angle x-ray scattering (GISAXS) and grazing incidence ultrasmall angle x-ray scattering (GIUSAX) overcome the limitations of conventional small angle and ultrasmall angle x-ray scattering studies as regards extremely small sample volumes (submonolayer regime) in the thin film geometry. Measurements were performed at the BW4 USAX beamline of the DORIS III storage ring at HASYLAB (DESY, Hamburg). The selected wavelength was $\lambda = 0.138$ nm. For GISAXS the instrument is operated in a reflection geometry (further details concerning the beamline are given in [37]). GISAXS experiments require a q_y resolution which increases the complexity in the experimental realization. In a high resolution set-up a typical resolution

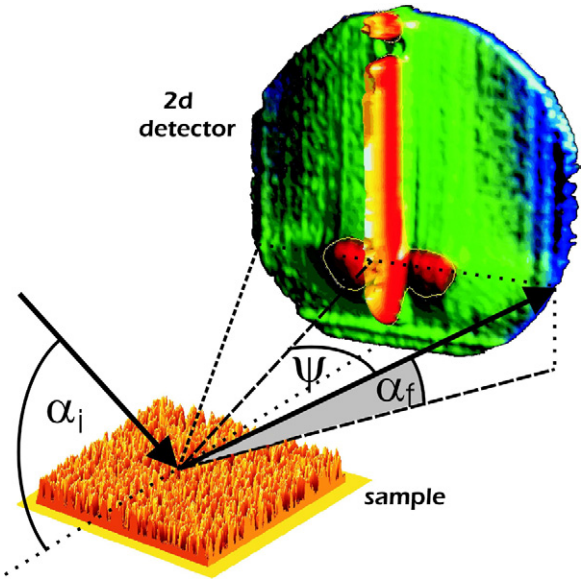

Figure 2. A schematic picture of the experimental set-up for the detection of diffuse scattering with a two-dimensional detector in the GISAXS geometry. The sample surface is placed horizontally. A typical phase separation structure as measured with SFM is shown, representing the sample surface. The incidence angle is denoted as α_i, the exit angle as α_f and the out-of-plane angle as ψ. The two-dimensional detector resembles along the horizontal axis the q_y dependence and along the vertical axis the q_z dependence (neglecting the small q_x contribution). The colour coding (low intensities in black and high intensities in white) visualizes differences in the scattered intensity on a logarithmic axis. In the particular example chosen, the diffusely scattered intensity in the scattering plane, the detector scan, exhibits a split Yoneda peak and a specular peak as common features of a nanostructured surface.

of $\delta q_y = 1.4 \times 10^{-3}$ nm^{-1} is realized. However, the theoretical description simplifies and lateral structures of one effective interface are directly accessible [38].

The beam quality was optimized by using a set-up of high quality entrance cross-slits and a completely evacuated pathway. Only one Be window separated the storage ring from the detector side. By avoiding any additional windows, the background was minimized. To enlarge the accessible wavevector range, different sample–detector distances were operated. At a small distance of for example 1.9 m, length scales between 6 and 380 nm can be resolved (GISAXS mode) and at a large distance of 12.8 m, these intervals are shifted to 39 and 2500 nm (GIUSAX mode) respectively. The scattered intensity was recorded with a two-dimensional detector consisting of a 512 × 512 pixel array (see figure 2). At one fixed incidence angle α_i, the two-dimensional intensity distribution can be cut into several slices vertical and horizontal with respect to the sample surface [39]. The GISAXS/GIUSAX information is extracted from the horizontal slices [40]. The intensity was integrated over a small slice Δq_z in the vertical direction. To ensure an easy separation of the specularly and the diffusely scattered intensities, an incidence angle α_i above the critical angles of the polymers as well as that of the substrate material was chosen (for a detailed description referring to polymeric samples, see [41]).

2.7. Grazing incidence small angle neutron scattering (GISANS)

The grazing incidence small angle neutron scattering (GISANS) experiments were performed at the D22 beamline (ILL, Grenoble). We used fixed wavelengths between 0.6 and 1.4 nm

(wavelength selector $\Delta\lambda/\lambda = 10\%$) to operate the instrument in the wavelength regime of the highest available neutron flux. Such as at the BW4 beamline at the D22 beamline usually transmission experiments were performed (detail concerning the beamline in [42]). Using the two-dimensional detector (128×128 pixel array) and a sample–detector distance of 17.66 m, a resolution comparable to that of the synchrotron radiation experiments was achieved. Originating from the different interactions of neutrons and x-rays with the sample system, the scattering contrast is now reversed as compared to that of GISAXS. Further principal ideas of GISANS and GISAXS are the same and are described above.

3. Sample preparation

For the model system of polystyrene (PS), polyparamethylstyrene (PpMS) and the diblock copolymer of the two homopolymers poly(styren-block-paramethylstyrene) (P(S-b-pMS)), ultrathin films were prepared on solid coated supports. We investigated pure native oxide covered silicon (100) substrates as well as polyamide and polyimide coated ones. Prior to the coating and to the preparation of the PS, PpMS, PS:PpMS and P(S-b-pMS) films, the substrates were cleaned to ensure reproducibility of the experimental results. A detailed description of the influence of substrate cleaning is given in the [43, 44]. Substrates directly subjected to spin coating of the polymer films under investigation (PS, PpMS, PS:PpMS and P(S-b-pMS) films) were cleaned with an acid bath (100 ml 80% H_2SO_4, 35 ml H_2O_2 and 15 ml deionized water for 15 min at 80 °C). To enable the preparation of polyamide [45] and polyimide [46] films with smooth and homogeneous surfaces, a basic cleaning (700 ml deionized/Millipore water, 60 ml H_2O_2 and 60 ml NH_3 for 2 h at 75 °C) of the silicon substrates was necessary. A homogeneous amorphous polyamide 6,I (PA) coating layer was obtained by spin coating with a 1,2-chlorphenol solution for 120 s at 1950 rpm. Amorphous PA from Bayer AG (Leverkusen, Germany; trademark: Durethan T40) with a molecular weight $M_w = 28\,900$ g mol^{-1} ($M_w/M_N = 3.28$, $T_g = 130$ °C) was used. Polyimide (PI) films resulted from a spin coating with *N*-methylene-2-pyrrolidone solution (120 s at 8000 rpm) and subsequent annealing. The annealing was carried out for 30 min at 200 °C; this was followed by 60 min at 350 °C and a slow cooling down to room temperature. PI was obtained from HD MicroSystems GmbH (Bad Homburg, Germany; trademark: Pyralin PI 2610).

Deuterated PS with a molecular weight $M_w = 157$ kg mol^{-1} ($M_w/M_N = 1.09$, $R_g = 10.6$ nm) as well as PpMS with a molecular weight $M_w = 157$ kg mol^{-1} ($M_w/M_N = 1.06$, $R_g = 10.0$ nm) were used in an asymmetric blend composition of PpMS:dPS = 3:2. The symmetric diblock copolymer P(S-b-pMS) had a molecular weight $M_w = 230$ kg mol^{-1} ($M_w/M_N = 1.08$) and a styrene fraction of the copolymer of $f_{PS} = N_{PS}/N = 0.47$. Additionally, homopolymer samples of dPS and PpMS were prepared for comparison. To prepare ultrathin films, highly diluted toluene solutions were used for the spin coating (30 s at 1950 rpm). Several samples were prepared from the same solution. By means of x-ray reflectivity the film thickness of the samples was measured and using SFM the surface morphology was determined right after preparation. Films are referred to as 'ultrathin' in the regime of thicknesses smaller than the radius of gyration of the unperturbed molecule R_g. From the polymer–polymer interaction parameter of deuterated PS and PpMS, $\chi = A + B/T$ with $A = -0.011 \pm 0.002$ and $B = 6.8 \pm 1$ K [47], a weak incompatibility as compared to those for other blend systems such as PS and brominated PS [29, 48] or polymethylmethacrylate [20] results. The diblock copolymer system investigated belongs to the strong segregation regime [49] due to having a value of $\chi N \sim 24.0$

For the creation of the reported surface morphologies, the as-prepared samples were stored for several hours in a toluene vapour atmosphere. Temperature and pressure were adjusted

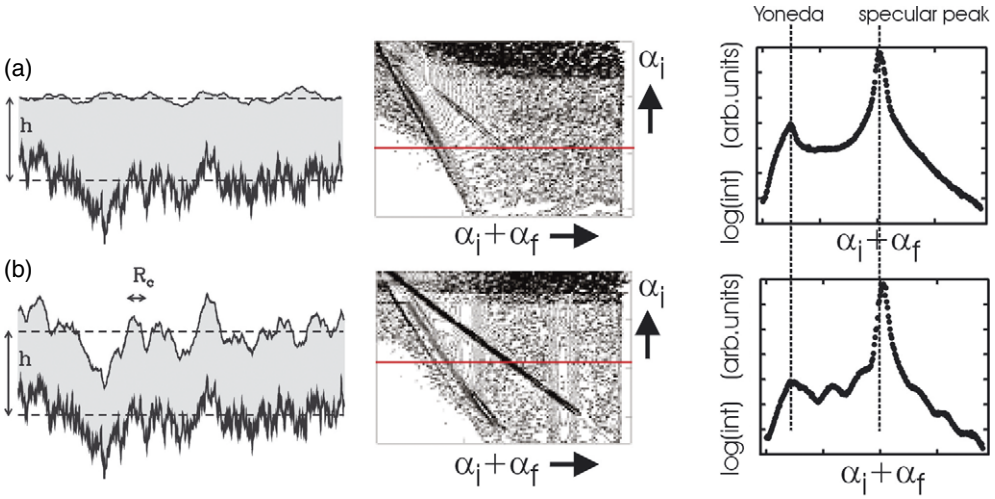

Figure 3. Schematic pictures of (a) uncorrelated and (b) partially or fully correlated interfaces. On the left-hand side, a coated substrate with a polymer film (light grey) on top is shown in a side view. In the central part a reciprocal space mapping in an angular representation is plotted as an example, for both interface types. The horizontal line represents one detector scan taken at a fixed incidence angle α_i displaying the intensity as a function of the detector angle $\alpha_i + \alpha_f$ yielding the right-hand graphs. In the single-detector scans the Yoneda and specular peak positions are emphasized by the dashed lines.

in a special vapour chamber. After the exposure time, the samples were rapidly quenched in ambient air. During storage, the samples might be sensitive to mechanical perturbations. To avoid structure formation by mechanically amplified gravitational surface waves (long wavelength waves of the order of hundreds of micrometres [50]), the vapour chamber is placed on an active vibration damping system. To check the reproducibility of the results reported, several samples were prepared and investigated.

4. Homopolymer film structures

Right after the preparation by spin coating, with GISAXS and GISANS a very special type of thin film behaviour was observed [51–55]. The homopolymer films acted as a band-pass filter and part of the roughness spectrum of the underlying substrate is transferred through, dominating the surface roughness of the polymer film. Figure 3 visualizes the differences between (a) uncorrelated and (b) partially or fully correlated interfaces in the case of a coated substrate with a polymer film on top.

For a sample with uncorrelated interfaces all interfaces scatter independently and the diffuse intensities of all individual interfaces superpose. The case of partially or fully correlated roughness gives rise to scattering with partial coherence, the resonant diffuse scattering (RDS) [56]. The partial phase coherence of the waves diffusely scattered from different interfaces concentrates the intensity in narrow sheets in reciprocal space. These sheets of resonant diffuse scattering are oriented parallel to the q_x axis with the centre fulfilling the one-dimensional Bragg condition [57] $\Delta q_z = 2\pi/d^{\mathrm{corr}}$. The modulations of the resonant diffuse scattering are in phase with the fringes of the reflectivity and show the distance d^{corr} of the correlated interfaces. In a detector scan, the RDS becomes visible as a modulation in the intensity, present in addition to the common features: the specular and the Yoneda peaks [58] (see figure 3).

For PS below the entanglement molecular weight M_e, the polymer surface has no correlation with the substrate surface. For above M_e, the two interfaces are correlated [51]. This correlation extended over a rather large range of film thicknesses h, starting in the highly confined regime $h \sim R_g/3$ and going up to $h \sim 18R_g$. At a film thickness of $26R_g$ an individual scattering of the interfaces was observed [54]. However, the exact number $X \times R_g$ will depend on the detailed experimental conditions of the sample preparation such as substrate cleaning and solvents used [55]. In the melt ($T > T_g$ or due to toluene vapour storage), this correlation vanishes and is not reinstated, because it forces the molecules to an energetically unfavourable conformation [52]. In the case of coated silicon substrates with a PA film on top, no roughness correlation was detected, which was attributed to a reduced substrate interaction [54]. Any observed long ranged correlation decayed with a small time constant as compared to those for typical dewetting kinetics. Thus before the onset of dewetting, the surface morphology initially produced by spin coating is lost. The liquid polymer surface is dominated by thermally excited waves [59].

In the case where the van der Waals interaction of the polymer molecules and the substrate atoms is small as compared to the interaction between the polymer molecules themselves, the long range part of the effective interface potential $f''(h)$ destabilizes the polymeric film. An unstable film, fulfilling $f''(h) < 0$, decays via spinodal dewetting [60, 61]. Among all of the unstable modes of the thermally excited waves, the fastest growth mode, with a wavevector $q_m = \sqrt{(3/2)}(a/h^2)$, destroys the film, where h denotes the film thickness and a a molecular length which depends on the van der Waals interaction [62]. In the metastable case, the system has to overcome a potential barrier in order to reach its state of lowest energy. The film ruptures due to a nucleation process. Far away from the sign reversal of $f''(h)$ the presence of nucleation sites (heterogeneous nucleation) is required, but otherwise a thermal activation can be sufficient to overcome the energy barrier (homogeneous nucleation). However, in the final state the destabilized film has decayed into an assembly of isolated drops. Thus dewetting as a structure directing mechanism results in drop morphology only.

Homopolymer systems such as PS on top of silicon substrates covered with an oxide layer have been frequently examined by many groups [63–80]. The applied surface cleaning strongly influences the observed behaviour as regards instability [43]. From the long ranged part of the effective interface potential, an absence of instability results as long as the PS film is thick as compared to the oxide layer thickness, because PS is stable on Si but unstable on silicon oxide [74–76]. Restricting consideration to ultrathin films with thicknesses $h < 2R_g$ (confinement regime), the film thickness becomes comparable to the oxide layer thickness and the short range part of the effective interface potential can no longer be neglected. Moreover, the calculation of Aubouy suggested that ultrathin polymer films dewet surfaces that thick films wet [81]. Due to the small molecular weight chosen ($R_g = 1.2$ nm for 2k), the confinement regime was not touched in the investigation of Seemann *et al* [75]. Entering this regime, in the case of 4k PS, Xie *et al* [78] observed instability of films with thicknesses below 10 nm. Rehse *et al* [82] observed an instability–stability transition of PS (molecular weights between 5.6k and 1000k) on corrugated as well as on flat Si substrates at a critical thickness $0.55R_g$. For the molecular weight chosen in this investigation (157k), ultrathin films were unstable if subjected to annealing above the glass transition temperature or to toluene vapour storage [70, 83]. Figure 4 shows data for PpMS homopolymer films after 7 h of toluene vapour storage.

As visible by SFM, due to the small size, the surface is covered with small droplets of polymeric material (see for example figure 4(a) for $h = 4.4$ nm). In an optical analysis the samples just looked like bare silicon. A contact angle of 6° results. In view of the ratio between the droplet height F and droplet diameter $2R$, a pancake model best describes the shape. However, the droplet diameter is not monodisperse, as observed in the case of PS in

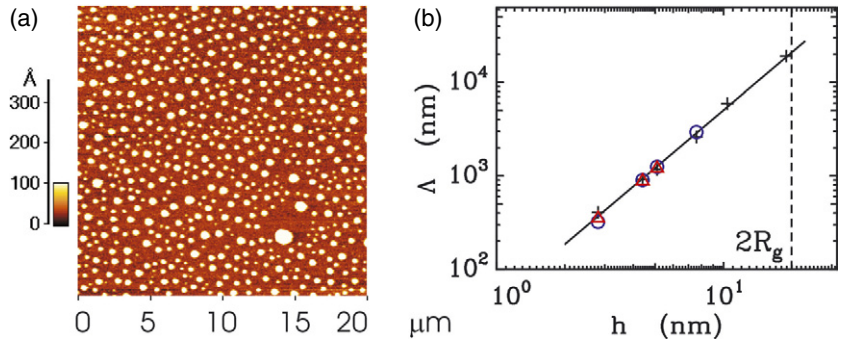

Figure 4. Dewetting of ultrathin PpMS films on native oxide covered Si surfaces. (a) Typical droplet structure as observable with SFM (scan range 20×20 μm^2) for an initial film thickness of 4.4 nm. (b) The most prominent in-plane length determined from the PSD calculated from SFM data (crosses), from GISAXS (circles) and from GISANS (triangles). The solid line follows $\Lambda \sim h^2$. The dashed line indicates the thickness $h = 2R_g$. The symbol size gives an indication of the experimental errors.

previous investigations as well [70]. As a consequence, in the PSD of the SFM data only one pronounced peak is observable. Its most prominent in-plane length Λ corresponds to the droplet distance. With respect to scattering it is structure factor information. For GISAXS and GISANS experiments, the structure factor peak is observed as well. Thus, with increased statistical significance as compared to SFM results, GISAXS and GISANS data confirm the presence of a dominant lateral length. With increasing initial PpMS film thickness h, it increases as well (see figure 4(b)). The solid line is a model fit to the data obeying $\Lambda \sim h^2$. Within the experimental error the data are describable with this power law. It should be noted that the confinement regime is rather limited by the accessible range of initial film thicknesses. The upper limit is given by $2R_g = 20$ nm (imposed by the molecular weight) and the lower limit by the size of the smallest stable continuous film that can be prepared, which is for the present example 2.8 nm [43]. Thus the typical range of several orders of magnitude necessary for extracting scaling behaviour is not realizable. Detection of intermediate stages of film destabilization, which are characterized by the presence of initial holes or a polygonal pattern, was impossible. Consequently, due to the lack of kinetic information, the destabilization mechanism (spinodal dewetting or nucleated dewetting) was not determined. The scaling extracted would be compatible with a spinodal dewetting (valid for the early stages), keeping in mind that a significant lateral coarsening of the structures is unlikely due to the very small film thickness [72]. However, knowledge of the power law allows one to control the thin film morphology.

Restricting consideration to homopolymers only, an increase in the complexity of the system is gained by increasing the oxide layer thickness or by adding a second coating layer. Polymeric coating layers have been used in many investigations focusing on the non-confined films on them [44, 45, 84–100].

In the case of PS on PA, both layers can be prepared directly by two subsequent spin coating steps [44, 45, 98, 99] because of the immiscibility of the solvents used. To use spin coating for the preparation of the top layer, it is essential to address only the ultrathin film regime. In addition, this minimizes the increase in impurity as compared to other bilayer preparation techniques such as floating. Upon PA layers of 40 nm thickness, confined dPS films were prepared (deuterated, 9k, $R_g = 2.7$ nm). After toluene vapour storage, again a droplet structure is observed (see figure 5(b)). A storage time of 8 h was selected. Again, the droplet

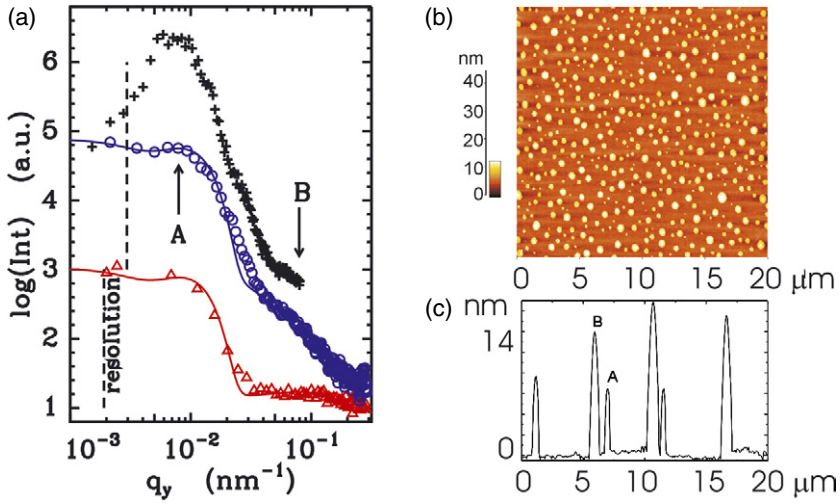

Figure 5. Dewetting of ultrathin dPS films ($h = 1.9$ nm) on PA coated Si surfaces. (a) A double-logarithmic plot of horizontal slices cut from the two-dimensional intensity distribution of the confined dPS sample dewetted during toluene storage. The dashed lines indicate the resolution limits of the individual experiments. Within the resolvable length scale range, the two most prominent in-plane lengths Λ are detected (positions marked 'A' and 'B') with GISAXS (circles) as well as with GISANS (triangles). Solid lines are fits. For comparison, the radially averaged PSD master curve calculated from SFM data (crosses) is shown. All curves are shifted for clarity along the intensity axis. (b) Typical droplet structure as observable with SFM (scan range 20×20 μm^2). (c) A representative line scan from the SFM data indicating the two different droplet populations.

diameters are not monodisperse and the shape corresponds to a pancake-type one. However, in contrast to the observations without the intermediate polymeric layer, two populations of droplets are detected. In the case of the thinnest dPS film examined, from the SFM pictures and the extracted line scans (see figure 5(c)) it might be difficult to distinguish between a two-stage droplet population and a broad distribution of droplet radii. In contrast, in reciprocal space, clearly two structural features were probed. As shown in figure 5(a), with GISANS and GISAXS the two most prominent in-plane lengths are detected.

Consequently, the resulting scaling behaviour becomes more complex as compared to that of samples without a PA layer. With increasing initially prepared dPS film thickness, after toluene vapour storage the ratio between the sizes of the emerging droplets changes. The small droplets (labelled 'B' in figure 5(a)) remain constant in size, whereas the larger ones (labelled 'A' in figure 5(a)) increase with increasing initial film thickness h. Accordingly, for films close to the upper limit of confinement $h \sim 2R_g$, the large droplets become observable with OM because of their size having increased above the optical resolution limit. Figure 6(a) shows an example. Its inset shows the related Fourier transform indicating the remaining spatial correlation. The observed scaling is summarized in figure 6(b). The most prominent in-plane lengths are plotted as a function of the initial film thickness. The horizontal solid line indicates the independence of the small droplets with respect to changes in h. The second solid line is a model fit to the data obeying $\Lambda \sim h^2$ again. Within the experimental error the data are describable with this power law in the case of $h < 2R_g$. Thus, irrespective of the presence or absence of a PA layer, an ultrathin destabilized homopolymer film agrees in its spatial correlations with the spinodal dewetting model. However, again a kinetic investigation was not possible and therefore a direct proof is lacking.

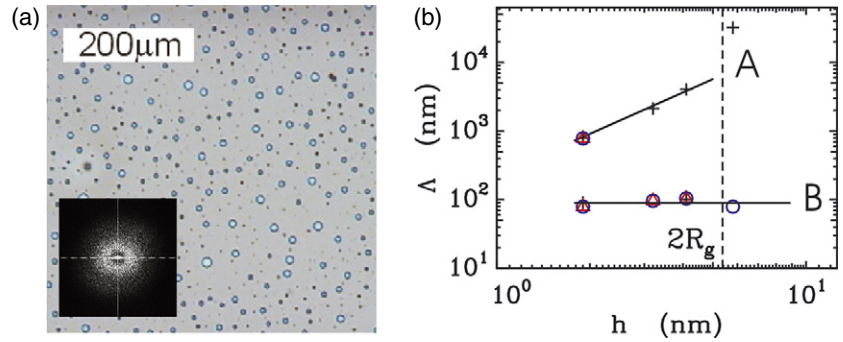

Figure 6. (a) Typical droplet structure as visible with OM (scale bar 200 μm), as measured for an initial film thickness of 4.1 nm. The inset shows the Fourier transform. (b) The most prominent in-plane length determined from the PSD calculated from SFM or OM data (crosses), from GISAXS (circles) and from GISANS (triangles). The upper solid line (A) follows $\Lambda \sim h^2$ and the horizontal one (B) obeys $\Lambda =$ constant. The dashed line indicates the thickness $h = 2R_g$. The symbol size gives an indication of the experimental errors.

Even within the experimental error for larger dPS film thicknesses, the data do not fit on the line $\Lambda \sim h^2$ extracted from the ultrathin film regime (not all shown in figure 6(b)). In addition, the type of spatial arrangement of the dPS droplets changes into the polygonal type, which was first observed by Reiter [72]. The polygonal arrangement of polymeric material can be modelled with Voronoi tesselations and thus indicates the presence of a nucleation and growth process driving the dewetting. This might be taken as an indication of a first-order transition in the dewetting behaviour [44]. It results from the more complex shape of the effective interface potential $f''(h)$ due to the added PA layer. The effective Hamaker constant $A_{\rm eff}(h)$ parametrizing the strength of the long ranged interaction $f_{\rm vdW}(h) = A_{\rm eff}(h)/(12\pi h^2)$ reflects the increased complexity. In the case of a polymeric bilayer (dPS on PA) on a coated substrate, the effective Hamaker constant depends on the thickness $d_{\rm ox}$ of the oxide coating layer covering the substrate and the thickness of the polymeric coating layer $h_{\rm PA}$:

$$A_{\rm eff}(h) = A_{\rm PAl} - A_{\rm ll} - \frac{A_{\rm lPA} - A_{\rm lox}}{(1 + h_{\rm PA}/h)^3} - \frac{A_{\rm lox} - A_{\rm ls}}{(1 + (d_{\rm ox} + h_{\rm PA})/h)^3}. \tag{1}$$

$A_{\rm ll}$, $A_{\rm lPA}$, $A_{\rm lox}$ and $A_{\rm ls}$ denote the Hamaker constants of the polymer (dPS), the polymer and the PA layer, the polymer and the oxide layer, and the polymer and the Si substrate. $A_{\rm PA} < A_{\rm PS}$ [44]. As long as the PA layer thickness is larger than the destabilized dPS layer thickness, the condition $f''(h) < 0$ is fulfilled and the dPS layer can decay via spinodal dewetting [44]. Consequently, the stability analysis likewise favours a spinodal dewetting scenario for the ultrathin films.

The short range contribution of the effective interface potential $f''(h)$ explains the existence of the second droplet species. Along the lines of the explanation given in [71], the interplay between short and long ranged contributions yields a two-step dewetting process due to an additional minimum in $f''(h)$. Its position and therefore also the size of the second, smaller droplet structure depend on the thicknesses of the oxide and the PA layers. As long as it is fixed, a structure with fixed size irrespective of the initially prepared film thickness occurs.

In summary, although the complexity is increased, again control of the thin film morphology is obtained from the extracted power law behaviour.

The chosen boundary condition of enabling direct bilayer preparation with a subsequent two-step spin coating limits the available variety of polymer pairs. Sticking to the destabilization of a PS homopolymer layer, the polymeric coating layer PA is replaced by PI.

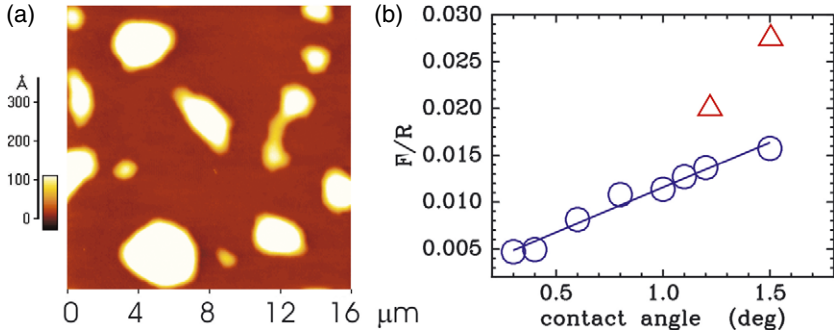

Figure 7. (a) Typical droplet structure as observable with SFM (scan range $16 \times 16\ \mu m^2$) observed during dewetting of PS on PI. (b) Scaling of the droplet shape F/R as a function of the contact angle. Data on the PS–PI bilayer (circles) are compared to those from the PS–PA bilayer (triangles). The solid line is a linear fit to the PS–PI data. The symbol size gives an indication of the experimental errors.

As a consequence, the main sample preparation is not modified. However, on replacing PA with PI the van der Waals interaction is changed. Since $A_{PI} < A_{PS}$ is still fulfilled, the complete argumentation presented for the case of a PA layer is transferable to the second type of bilayer film examined (PS on PI). The full experimental investigation can be reapplied and summarized in terms of a power law behaviour. Nevertheless, replacing PA by PI yields changes which are better accounted for in an analysis of the resulting droplet shapes rather than spatial correlations.

Figure 7(a) shows an example of the kinds of PS droplets on PI resulting from the destabilization by toluene vapour storage (storage time 8 h). Just like in the observations in the case of PS on PA, two populations are detected (small and large droplets). The shape of the sessile droplet at the solid PI surface is obtained from the functional variation of the Hamiltonian with the field variable. In the effective interface model approach, the field variable denotes the local height $z(r)$ of the liquid–vapour interface above the solid. An assumed cylindrical symmetry is expressed in the radial dependence r of the droplet height z. As figure 7 indicates, this assumption is not a meaningful approximation for all experimentally observable droplets. Therefore the analysis of the droplets probed is restricted to nearly cylindrical ones.

In the case of rather macroscopic drops, in the limit of vanishing chemical potential difference between the bulk liquid and the vapour phase, the ratio of the drop height F and the drop radius R follows $F/R = \sqrt{|S|/(2\gamma)}$, with γ the liquid–vapour surface tension [74]. Hence, with $S = \gamma\Theta^2/2$ it depends linearly on the contact angle Θ. Seemann *et al* [74] observed, in the case of PS (2k, 4–15 nm thickness) on OTS coated Si substrates, a good agreement as long as the contact angles are small. Thus the squared-gradient expression of the surface free energy characterized the PS droplet shape well. In contrast, for larger contact angles the shape becomes spherical cap-like [74]. Figure 7(b) visualizes the scaling of the drop shape as a function of the contact angle in the case of PS on PI and PA. Because only the ultrathin film regime is addressed, the resulting droplets were rather small, yielding small values of F/R. The contact angles are rather small as well, due to the small differences between the Hamaker constants of PS and PI or PA. The solid line is a linear fit to the data (PS on PI). Thus the scaling of the droplet shape is in agreement with the simple theoretical model. The two available data points in the case of PS on PA do not match with this line. The shape of the droplets probed is different in qualitative behaviour. However, due to the lack of more data, a scaling is not extracted.

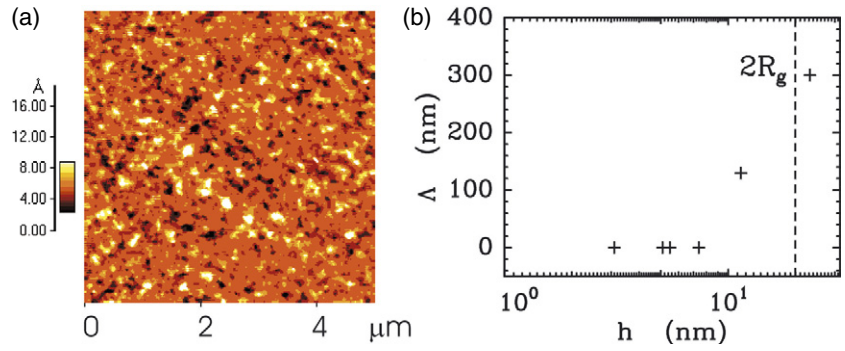

Figure 8. The characteristic in-plane length Λ as a function of the polymer blend film thickness l for as-prepared samples in the confinement regime. (a) Typical phase separation structure as observable with SFM (scan range $5 \times 5\ \mu m^2$) for an initial film thickness of 23.2 nm. Note that the morphologies are created at a film thickness which is larger than $2R_g$. (b) The most prominent in-plane length determined from the PSD calculated from SFM data (crosses). Master curves for SFM data which exhibit no peak in the entire measured q range were plotted with $\Lambda = 0$. The dashed line indicates the thickness $h = 2R_g$. The symbol size gives an indication of the experimental errors.

In summary, a structure best described as droplets is the only morphology observable in the case of ultrathin homopolymer films. As a consequence, with one number, the most prominent in-plane length Λ (the distance between the droplets), the morphology is fully statistically described for the lateral direction. Control is gained by precise preparation of the initial film thickness. From the scaling laws determined, its value can be adapted to the desired lateral structure size. A fine tuning of the exact droplet shape is accessible via a variation of the substrate layering. Thus control of the exact droplet shape is obtained by designing the full polymeric system in terms of the sacrificial top layer, which is transformed into droplets via dewetting, and the sublayer, which modifies the effective interface potential.

5. Polymer blend film structures

Replacing the homopolymer film with a blend film enriches the variety of surface patterns observed after thin film preparation by spin coating [101, 102, 20]. Roughness replication is still one possible surface feature [48], but in addition dominant surface structures result. Different blending ratios of the two polymers PS and PpMS give rise to surface structures which are describable as smooth films, holes, continuous patterns, droplets and smooth films, again while changing the volume fraction of the one-component PS ϕ_{PS} from 0 to 1 [14, 26]. With decreasing concentration of the polymer used for the spin coating, the lateral size of the structures reduces [103]. A comparable effect is achievable by reducing the effective polymer–polymer interaction parameter χ [29], which is however fixed for the system PpMS:PS.

Entering the regime of confined thin films changes the behaviour. In figure 8 the most prominent in-plane length as extracted from the SFM data is plotted as a function of the blend film thickness. The absence of a surface pattern yields a master curve without any peak of intensity in Fourier space and is identified with $\Lambda = 0$ in figure 8 [103]. For films with thickness $h < R_g$ no surface features were detected. However, roughness correlation still connects the statistical roughness of the substrate to that of the thin film surface. Figure 8(a) shows the weakly modulated surface observable in the case of $h = 23.2$ nm $> 2R_g$. Laterally separated phase domains present in solvent-quenched thin films (resulting from a spin coating process)

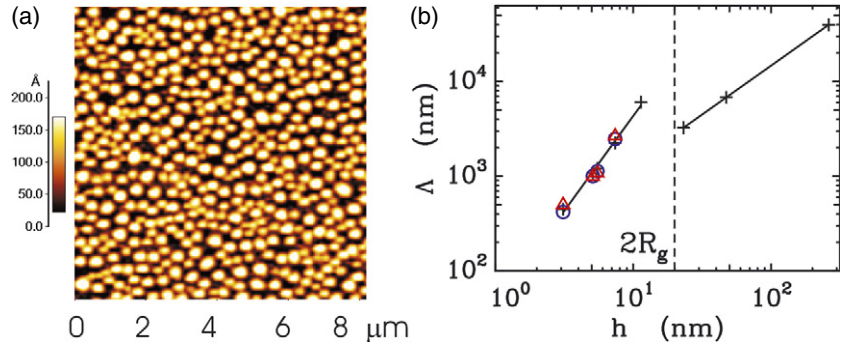

Figure 9. Dewetting of ultrathin PpMS:dPS blend films on native oxide covered Si surfaces. (a) Typical droplet structure as observable with SFM (scan range $9 \times 9\ \mu m^2$) for an initial film thickness of 3.1 nm. (b) The most prominent in-plane length determined from the PSD calculated from SFM data (crosses), from GISAXS (circles) and from GISANS (triangles). The solid line follows $\Lambda \sim h^2$ in the confined regime and $\Lambda \sim h^1$ elsewhere. The dashed line indicates the thickness $h = 2R_g$. The symbol size gives an indication of the experimental errors.

are always accompanied by free surface undulations [104]. The surface undulations are related to the different rates of evaporation of the solvent from various blend phases [105, 106]. This is a consequence of the different solubilities of various polymers in their common solvent. The solvent evaporates faster from the phase rich in less soluble polymer, which solidifies earlier. In turn, the phase rich in more soluble polymer is swollen. As the solvent evaporates finally also from this phase, there is a collapse and the lower regions of the free surface are built. This total mechanism takes place during the third stage of spin coating [105]. Thus the absence of surface modulations is explainable by the small differences in solubility of PS and PpMS in the solvent used, toluene. In addition, on the basis of a mean field treatment it was theoretically predicted that with decreasing film thickness the polymer–polymer interaction parameter is decreased as well [107] and thus polymer blend films become more compatible [108], supporting the suppression of any surface feature. Because PS and PpMS in the bulk are already only weakly incompatible, it might be reasonable to suggest that this non-monotonic behaviour originates from a spatial restriction of the film thickness, which suppresses the lateral phase separation for $l < R_g$.

After toluene vapour storage (7 h), pronounced surface patterns were observed irrespective of the initially prepared film thickness and thus irrespective of the type of surface structure present after spin coating [83]. In general, two different types of structure resulted. For films with thickness $h < 2R_g$, polymeric droplets on the solid support were present, as shown for example in figure 9(a). Similarly to the pure homopolymer case, in view of the ratio between the diameter and height the shape is best described as pancake-like. In contrast, films with $h > 2R_g$ showed a continuous surface pattern commonly observed in the case of the most nearly symmetric blend thin film systems (see figure 1(a)). Due to the toluene vapour storage, the structure coarsened but was still continuous. The surface patterns detected are very similar to the ones calculated ones on the basis of a lattice Boltzmann simulation with conserved order parameter [109]. In the case of high viscosity and negligible hydrodynamic flow, the experimentally observed morphologies fit well to the calculated ones. This strongly suggests that in the case of the blend system PpMS:dPS, examined in this investigation, the coarsening during the toluene vapour storage is not dominated by hydrodynamic flow. Thus, during the plastification the viscosity was still so high that hydrodynamic flow could be neglected. In contrast, for surface structures in spin coated PMMA:PS blend films, hydrodynamic flow was

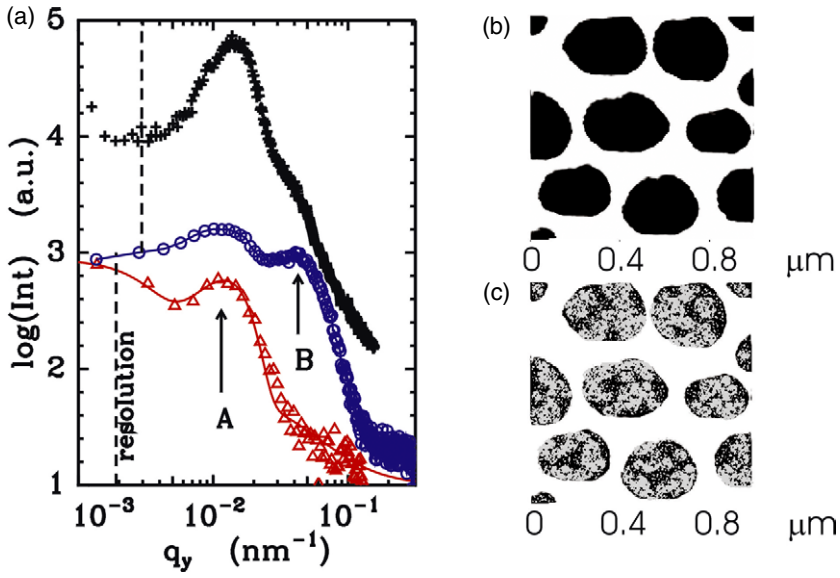

Figure 10. (a) A double-logarithmic plot of horizontal slices cut from the two-dimensional intensity distribution of the confined PpMS:dPS sample ($h = 3.1$ nm) dewetted during toluene storage. The dashed lines indicate the resolution limits of the individual experiments. Within the resolvable length scale range, either one or two most prominent in-plane lengths Λ are detected (positions marked 'A' and 'B') with GISAXS (circles) as well as with GISANS (triangles). Solid lines are fits. For comparison, the radially averaged PSD master curve calculated from SFM data (crosses) is shown. All curves are shifted for clarity along the intensity axis. (b) The calculated model of the scattering length densities as 'seen' by x-rays in GISAXS. Contrast is only yielded between polymer (black) and vacuum (white). (c) A tentative model of the scattering length densities of dPS (black) and PpMS (grey), as 'seen' by neutrons in GISANS.

identified as the leading mechanism during the coarsening of the as-cast blend film [105]. The differences of the molecular weights of the systems investigated, which change the viscosity, as well as the change in the polymer–polymer interaction parameter might be contributary causes.

In the PSD of the SFM data, one pronounced peak is observable (denoted as 'A' in figure 10(a)). Depending on the degree of monodispersity of the droplets, a shoulder (denoted as 'B'), as a second feature, becomes visible [110]. The most prominent in-plane length Λ, calculated from the position of the pronounced peak, again corresponds to the droplet distance. With respect to scattering it is structure factor information. Similarly to the homopolymer samples case, in GISAXS and GISANS experiments this structure factor peak is observed as well (see figure 10(a)). Thus, with increased statistical significance as compared to SFM, GISAXS and GISANS data confirm the presence of a dominant lateral length (shown in figure 9).

In addition, in GISAXS the shoulder becomes more pronounced and becomes a second peak, revealing the fact that when using x-rays the blend system PpMS:dPS has nearly no contrast. In the complete in-plane projection of an GISAXS experiment, the pancake shape degenerates into circles (see figure 10(b)) and thus the form factor contribution is enhanced as compared to the SFM case, in which the pancake shape yields a smearing of the mean diameter as a function of the droplet height. Due to deuteration of the PS component, in GISANS the contrast is strongly enhanced and mainly only the deuterated component is visible. As a

consequence, with GISANS chemical sensitivity results and the organization of the blend components inside the droplets is accessible [83]. In the case of a regular phase separation structure which is repeated inside each individual droplet within the total illuminated surface area, a second dominant in-plane length would be introduced. In GISANS, this second length would be detectable and observable as a second peak [111]. Because of the location inside the droplets, the real space length would be smaller as compared to the droplet distance and thus in the GISANS data the expected second peak had to appear at larger q_y values as compared to the position of the structure factor peak. However, the GISANS data showed only one dominant peak corresponding to the droplet distance. Therefore no internal regular phase separation structure can be present inside the droplets. It is instead an irregular arrangement of the molecules, which differs from droplet to droplet in its individual structure (see figure 10(c)) and consequently the related scattering information is averaged to zero.

Remarkable, equal to the homopolymer films on top of native oxide covered silicon, one most prominent in plane length Λ is sufficient to yield a full statistical description. In figure 9(b) it is shown as a function of the initial blend film thickness. The solid line is a model fit to the data obeying $\Lambda \sim h^2$ for $h < 2R_g$ and $\Lambda \sim h$ for $h > 2R_g$. Within the experimental error the data are describable with this scaling. It should be noted that within the regime $h > 2R_g$ a larger data set was analysed [103], which is not shown because we restrict our consideration to confined films within this investigation. The limitation with respect to the accessible range of confined thin blend films is similar to the one described for the homopolymer samples (see the previous section). The droplet distance of confined films with $h < 2R_g$ agrees well with a spinodal model and that for the non-confined structures with typical phase separation structures (see figure 1(a)).

6. Diblock copolymer film structures

Instead of mixing, in a diblock copolymer the two homopolymers PpMS and dPS are chemically linked together and phase separation is replaced by microphase separation [12]. For symmetric diblock copolymers, in which the two blocks occupy equal volume fractions, a lamellar orientation is preferred [112].

With the spin coating technique, P(S-b-pMS) films were prepared which exhibited a roughness correlation between the substrate and the copolymer surface within a limited film thickness and molecular weight range right after preparation [113]. The transferred part of the roughness spectrum of the substrate is explained as a morphology of a frozen liquid with a surface bending rigidity comparable to that of simple homopolymer films. Due to the strong surface segregation of the PpMS component [114], a lamellar order was already installed right after preparation, irrespective of the long ranged correlation. Its periodicity is different as compared to the equilibrium bulk state case. During annealing, the energetically unfavourable roughness replication decayed and an internal ordering with a lamellar thickness comparable to that of the bulk was formed. The internal lamellar order prevents thin diblock copolymer films from dewetting in many sample systems [112]. As a consequence, thin diblock copolymer films basically show no tendency towards destabilization [115]. With decreasing film thickness the confinement gives rise to an interplay between the intrinsic length scale of the bulk structure (bulk lamellar period L_0) and the geometry of the film. This yields transitions between phases of identical symmetry but different orientation with respect to the confining walls. As an example, lamellar domains reorient from a parallel to a perpendicular arrangement [116].

With storage under toluene vapour, a destabilization of confined films with thicknesses $h < 2R_g$ is possible (storage time 12 h) [17]. Films with larger thickness remain stable and exhibit no sign of destabilization. Because $2R_g = 27.2$ nm $< L_0 = 45$ nm in confined

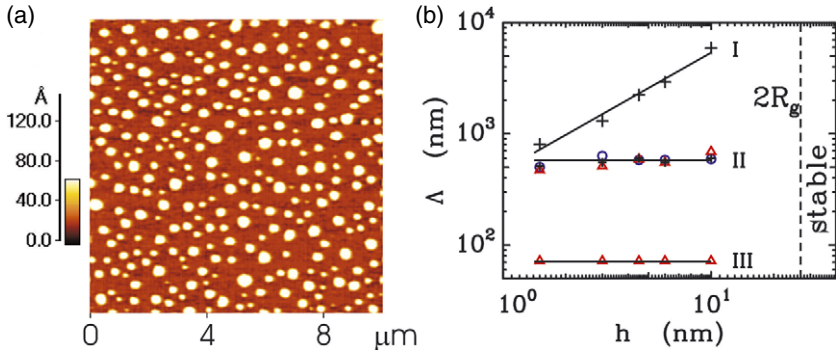

Figure 11. Dewetting of ultrathin P(S-b-pMS) diblock copolymer films on native oxide covered Si surfaces. (a) Typical droplet structure as observable with SFM (scan range $10 \times 10\ \mu m^2$) for an initial film thickness of 1.5 nm. (b) The most prominent in-plane length determined from the PSD calculated from SFM data (crosses), from GISAXS (circles) and from GISANS (triangles). The solid line describing structure type I follows $\Lambda \sim h^1$ and the structure types II and III are characterized by $\Lambda \sim$ constant. The dashed line indicates the thickness $h = 2R_g$. The symbol size gives an indication of the experimental errors.

films, no parallel oriented lamellar form is possible and the stabilization effect of the lamellar arrangement is not present.

With SFM, two types of droplet population on the surface are observed. Due to the asymmetries in the parameters defining the object shape (height $\ll$ diameter), the imposed shape is of pancake type again. The diameter of the large droplets increases with increasing amount of polymeric material present, while the diameter of the small droplets remains constant [17]. In the case of the thinnest sample examined, the two types are hardly distinguishable (see figure 11(a)), but they are present, as a careful statistical analysis shows. In the PSD calculated from the SFM data, one dominant most prominent in-plane length is detected, which corresponds to the large droplets. It yields a well pronounced peak (see figure 12(a)). The signature of the small droplets is visible at smaller q_y values and appears as a broad shoulder. The two structural types are referred to as 'I' and 'II' in figures 11(b) and 12. The large droplets (type 'I' structure) follow $\Lambda \sim h$ and the small droplets (type 'II' structure) follow $\Lambda =$ constant. Consequently, they are not in agreement with a simple spinodal mechanism, which would result in a scaling exponent of 2, as observed in the case of homopolymers and polymer blends (see the two previous sections).

To improve the statistical significance of the results from the SFM measurements, GISAXS and GISANS measurements were performed (see figure 12(a)). Moreover, the combination of the two techniques based on different probes enables a separation of surface and buried structures. Due to the lack of scattering contrast between PpMS and dPS in GISAXS, the structure resulting from the dewetting process is probed, whereas in GISANS, the strong contrast of the scattering length densities enables access to the internal microphase separation structure inside the large and small droplets.

Addressing surface features, the large droplets are not resolved in the GISAXS experiments. The shoulder in the GISAXS data confirms the shoulder in the SFM data and thus the existence of small droplets as a second structural surface feature. GISANS also confirms the existence of small droplets. In addition, GISANS yields a third structural feature not present in the SFM data and thus not related to a surface structure. In the GISANS data, at large q_y values a clearly visible peak occurs (marked 'III'). Due to the related real space length, it must result from a perpendicular arrangement of the diblock copolymer molecules inside the

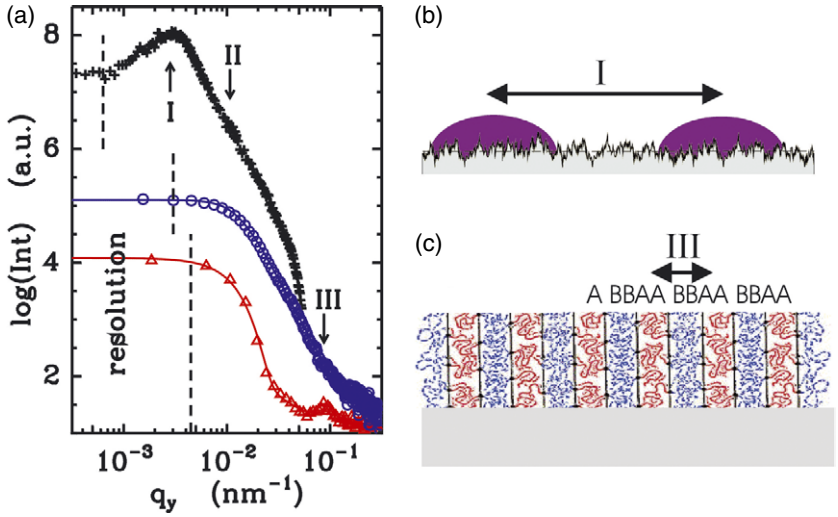

Figure 12. (a) A double-logarithmic plot of horizontal slices cut from the two-dimensional intensity distribution of the confined P(S-b-pMS) sample ($h = 4.5$ nm) dewetted during toluene storage. The dashed lines indicate the resolution limits of the individual experiments. Within the probed length scale range, three different most prominent in-plane lengths Λ are detected (positions marked 'I', 'II', 'III'). In the GISAXS (circles) as well as GISANS (triangles) data, due to the relaxed resolution, the largest one (marked 'I') is not resolved. Solid curves are fits. For comparison, the radially averaged PSD master curve calculated from SFM data (crosses) is shown. The smallest length is only observable with GISANS (marked 'III'). All curves are shifted for clarity along the intensity axis. (b) A schematic side view of the large droplet structure yielding the most prominent in-plane length 'I', revealed as the droplet distance. (c) A schematic view inside the droplets. From a microphase separation structure, a chemical contrast accessible to neutrons results, explaining the in-plane length 'III'.

large and small droplets with respect to the substrate surface. Within the experimental error, a value of 72 nm is obtained. No film thickness dependence or dependence on the droplet diameter is observed (see figure 11(b)). When compared to the value of the bulk lamellar spacing $L_0 = 45$ nm, this indicates a stretching parallel to the substrate surface.

To address the interplay between dewetting and microphase separation in more detail, a kinetic investigation of the evolving structures was performed [21]. Ultrathin film samples were exposed to toluene vapour to allow a time dependent investigation. The combination of GISANS, GISAXS and SFM data enabled the temporal separation of the two structure directing mechanisms [21]. In a first step, via nucleated dewetting a host structure of isolated polymeric islands is created [22]. In a second step, via a microphase separation process the polymeric material inside these islands is ordered, yielding the perpendicularly oriented lamellar structure. In addition, the shape of the host structure is transformed from an island type, deviating strongly from the cylindrical symmetry into droplets, as shown in figure 11(a). It is worth noting that the surface structures created by the toluene vapour treatment are stable against further annealing above the glass transition temperature. The pancake shaped droplets do not alter in shape or position, and the internal microphase separation structure is not modified [117].

In summary, with diblock copolymer film a hierarchical structuring of surfaces is obtainable by the destabilization of ultrathin films. Control of the thin film morphology is again gained from the extracted power law behaviour.

7. Discussion

From toluene vapour storage, irrespective of the type of polymer subjected to the solvent vapour, large scale isotropic surface structures resulted. From the applications point of view, structural isotropy is desired in all types of surface pattern, whose properties should not depend on the exact orientation (e.g. self-cleaning surfaces [119]). Isotropy is basically gained due to the absence of forces acting parallel to the substrate surface. It is worth noting that all reported structures have been prepared on large scale surfaces, such as typical Si wafers with 100 mm diameter. The strength of the reported technique is in manufacturing nanostructured films of this large extent via rather dedicated (surface cleaning) but simple (vapour storage) preparation routes. Proof of the homogeneity of the prepared surface pattern as regards the position on the full Si wafer was only accessible due to the scattering techniques applied. Real space techniques are always limited to surface areas of negligible size—as compared to the large Si wafer size. However, the real space techniques help as regards understanding the observed statistical information.

As compared to the growth of nanostructures, the preparation described, based on destabilization of initially homogeneous films, follows the reverse idea. In epitaxial growth [120] for example, molecular order results from the balance of the molecule–substrate and intermolecular interactions. However, neither the size of domains nor their spatial arrangement can be easily controlled. The basic reason is the non-equilibrium growth conditions [121]. In addition, coarsening phenomena occurring during growth such as static coalescence, Oswald ripening and nucleation, prevent the building of ordered patterns [122]. To achieve structural correlations, special growth conditions are required [123]. From homogeneous nucleation, droplet patterns are obtainable in the pure growth regime [124]. On the reverse path, ordered surface patterns result from homogeneous nucleation as well as from spinodal dewetting.

The ordered surface patterns result in spatial correlations which enable control of the thin film morphology via a statistical description. A disadvantage of the scaling laws is the lack of access to the underlying mechanism of the instability. Spatial correlation can occur in pure nucleation systems as well [124].

In a true random Voronoi mosaic, built on a Poisson-distributed seed, the analytical form of the droplet size distribution is a Gamma distribution [125]. Deviations from the random mosaic are already introduced by the presence of a selection rule of stable nuclei during the nucleation stage [126] and spatial correlations result. In a dewetting scenario a selection rule is defined by the shape of the free energy difference between the continuous film and a film with a hole, giving rise to the presence of a lower critical hole radius r_c [127, 128]. Holes with a smaller radius $r < r_c$ will be annealed and no dewetting is observable, although locally the surface is not wettable. In a simple approximation, the critical hole radius $r_c = h(1 + \sqrt{2})/(1 - \cos\theta)$ depends on the film thickness and the contact angle [128].

In contrast, simulated interface patterns of binary mixtures show no marked spatial correlations, although in the simulation a nucleation process was explicitly not included: a spinodal process was assumed [129]. The irregular size distribution of the simulated droplets together with the irregular arrangement is therefore no proof of a nucleation and growth process; rather, it results from a non-linear spinodal process.

Thus pure analysis of the finally established surface pattern is not suitable for the detection of the driving mechanism of instability. In principle, the detection of the kinetic evolution of the early stages, starting with the increase of the surface roughness caused by the change of the continuous initially prepared film, is required. However, in the ultrathin film regime, due to the interplay of rather fast kinetics as compared to thick films and the requirement of a high

spatial resolution for probing changes of the order of nanometres, kinetic investigations have not been commonly realized experimentally so far.

8. Summary

The destabilization of ultrathin (confined) polymer films turned out to be a powerful tool for use in preparation of isotropically patterned surfaces. The interplay between dewetting and phase separation or microphase separation controls the morphology of the resulting polymeric structures on a solid support. The effective interface potential of the solid support is tuned by a change of the silicon substrate coating. Dewetting as a structure directing mechanism creating a host structure results in a drop (or droplet) morphology only. Thus dewetting morphologies in the late equilibrium state are easily distinguished from e.g. phase separation and microphase separation structures. Thin (not ultrathin) film phase separation structures exhibit surface patterns with undulations [20] due to different solubilities. Microphase separation can cause the typical island structures originated by a frustration effect [12].

By combination of real and reciprocal space analysis techniques [118] the determination of statistically relevant numbers, characterizing the spatial correlations, was possible. From the extracted power laws the desired control of the thin film morphology, necessary for reproducibly preparing these kinds of nanostructured films for applications, was gained.

The most prominent in-plane length scales with initially prepared film thickness via $\Lambda \sim h^2$ in the case of homopolymer and polymer blend films that are destabilized. It changes to $\Lambda \sim h$ in the case of diblock copolymers as long as only the ultrathin film regime is addressed. The increase in complexity from homopolymers to polymer blends and diblock copolymers introduces the possibility of buried structures located inside the droplets caused by dewetting. In diblock copolymer films, driven by microphase separation a hierarchical structure resulted, which is well characterized by three different lateral lengths.

Acknowledgments

This work has benefitted strongly from fruitful and enjoyable collaborations with K Binder, Y-C Lin, M Müller and W Petry. The cooperation of M Casagrande, A Diethert, A Götzendorfer, N Hermsdorf, J Kraus, T Kuhlmann, V Lauter-Pasyuk, S Loi, C Lorenz-Haas, E Maurer, P Panagiotou, T Titz, P Volodin, H Walter and M Wolkenhauer in many experiments and stimulating discussions with R Blossey, H J Butt, M D Foster, K Graf, S Herminghaus, K Jacobs, A Karim, G Krausch, G Reiter and T Thurn-Albrecht are gratefully acknowledged. Support at HASYLAB was provided by S Cunis, M Dommach, W Fenzl, S S Funari, R Gehrke, G von Krosigk and A Meyer, at ILL by R Cubitt and at ESRF by M Burghammer, C Riekel, S Roth and D Smilgies. The silicon substrates used were kindly made available by Wacker Siltronic, Burghausen (Germany). Financial support was provided by the DFG in the framework of the priority programme 'Wetting and structure formation at interfaces' (Sta324/8).

References

[1] Fedynyshyn T H (ed) 2002 *Advances in Resist Technology and Processing XIX* (*Proc. SPIE* vol 4690) (Bellingham, WA: SPIE Optical Engineering Press)
[2] Russell T P 2002 *Science* **297** 964
[3] Ito H 1998 *J. Photopolym. Sci. Technol.* **11** 379

[4] Husemann M, Morrison M, Benoit D, Frommer J, Mate C M, Hinsberg W D, Hedrick J L and Hawker C J J 2000 *Am. Chem. Soc.* **122** 1844
[5] Chou S Y, Krauss P R and Renstrom P J 1996 *Science* **272** 85
[6] Whitesides G M, Mahias J P and Seto C T 1990 *Science* **254** 1312
[7] Aksay A, Trau M, Manne S, Honma I, Yao N, Zhou L, Fenter P, Eisenberger P M and Gruner S M 1996 *Science* **273** 892
[8] Thurn-Albrecht T, DeRouchey J, Jaeger H M and Russell T P 2000 *Macromolecules* **33** 3250
[9] Spatz J P, Möller M, Noeske M, Behm R J and Pietralla M 1997 *Macromolecules* **30** 3874
[10] Dietrich S 1988 *Phase Transitions and Critical Phenomena* vol 12 (New York: Academic)
[11] Israelachvili J N 1991 *Intermolecular and Surface Forces* 2nd edn (London: Academic)
[12] Hamley I W 1998 *The Physics of Block Copolymers* (Oxford: Oxford University Press)
[13] Findenegg G H and Herminghaus S 1997 *Curr. Opin. Colloid Interface Sci.* **2** 301
[14] Müller-Buschbaum P, Gutmann J S and Stamm M 1999 *J. Macromol. Sci.* B **38** 577
[15] Wang J and Composto R J 2003 *Interface Sci.* **11** 237
[16] Limary R and Green P F 1999 *Macromolecules* **32** 8167
[17] Müller-Buschbaum P, Wolkenhauer M, Wunnicke O, Stamm M, Cubitt R and Petry W 2001 *Langmuir* **17** 5567
[18] Lawrence C J 1988 *Phys. Fluids* **31** 2786
[19] Laschitsch A, Bouchard C, Habicht J, Schimmel M, Rühe J and Johannsmann D 1999 *Macromolecules* **32** 1244
[20] Geoghegan M and Krausch G 2003 *Prog. Polym. Sci.* **28** 261
[21] Müller-Buschbaum P, Cubitt R and Petry W 2003 *Langmuir* **19** 7778
[22] Müller-Buschbaum P, Hermsdorf N, Roth S V, Wiedersich J, Cunis S and Gehrke R 2004 *Spectrochim. Acta* B **59** 1789
[23] Born M and Wolf E 1964 *Principles of Optics* (Oxford: Pergamon)
[24] Biegen J F and Smythe R A 1988 *SPIE O/E LASE'88 Symp. (Los Angeles, CA)* (Bellingham, WA: SPIE Optical Engineering Press)
[25] Behm R J, Garcia N and Rohrer H (ed) 1990 *Scanning Tunneling Microscopy and Related Methods* (*Nato ASI Series E* vol 184) (Dordrecht: Kluwer)
[26] Müller-Buschbaum P, Gutmann J S and Stamm M 2000 *Macromolecules* **33** 4886
[27] Russ J C 1994 *Fractal Surfaces* (New York: Plenum)
[28] Bendat J S and Piersol A G 1971 *Random Data: Analysis and Measurement Procedures* (New York: Wiley–Interscience)
[29] Gutmann J S, Müller-Buschbaum P and Stamm M 1999 *Faraday Discuss.* **112** 285
[30] Lekner J 1987 *Theory of Reflection* (Dordrecht: Martinus Nijhoff)
[31] Bahr D, Press W, Jebasinski R and Mantl S 1993 *Phys. Rev.* B **47** 4385
[32] Stamm M and Schubert D W 1995 *Annu. Rev. Mater. Sci.* **25** 325
[33] Binder K 1983 *J. Chem. Phys.* **79** 6387
[34] Binder K and Frisch H 1984 *Macromolecules* **17** 2928
[35] Cubitt R 2001 *Opportunities for Neutron Scattering at the ILL in the Third Millennium* (Grenoble: Institut Laue–Langevin) p 279
[36] Cubitt R 2002 *Appl. Phys.* A **74** S329
[37] Gehrke R 1992 *Rev. Sci. Instrum.* **63** 455
[38] Salditt T, Metzger T H, Peisl J and Goerigk G 1995 *J. Phys. D: Appl. Phys.* **28** A236
[39] Salditt T, Metzger T H, Peisl J, Reinker B, Moske M and Samwer K 1995 *Europhys. Lett.* **32** 331
[40] Naudon A, Babonneau D, Thiaudiere D and Lequien S 2000 *Physica* B **283** 69
[41] Müller-Buschbaum P 2003 *Anal. Bioanal. Chem.* **376** 3
[42] Büttner H G, Lelievre-Berna E and Pinet F (ed) 1997 *Guide to Neutron Research Facilities at the ILL* (Grenoble: Institut Laue–Langevin) p 32
[43] Müller-Buschbaum P 2003 *Eur. Phys. J.* E **12** 443
[44] Müller-Buschbaum P, Bauer E, Lin Y C and Müller M 2004 at press
[45] Renger C, Müller-Buschbaum P, Stamm M and Hinrichsen G 2000 *Macromolecules* **33** 8388
[46] Hermsdorf N 2003 private communication
[47] Schnell R and Stamm M 1997 *Physica* B **234** 247
[48] Gutmann J S, Müller-Buschbaum P, Wunnicke O and Stamm M 2000 *Mater. Res. Soc. Symp. Proc.* **629** 6.1
[49] Helfhand E and Wassermann Z R 1980 *Macromolecules* **13** 994
[50] Wehausen J V and Laitone E V 1960 *Handbuch der Physik* Band IX *Strömungsmechanik III* ed H S Flügge (Berlin: Springer) p 446

[51] Müller-Buschbaum P and Stamm M 1998 *Macromolecules* **31** 3686
[52] Müller-Buschbaum P, Gutmann J S, Lorenz C, Schmitt T and Stamm M 1998 *Macromolecules* **31** 9265
[53] Kraus J, Müller-Buschbaum P, Bucknall D G and Stamm M 1999 *J. Polym. Sci. Phys.* **37** 2862
[54] Müller-Buschbaum P, Gutmann J S, Kraus J, Walter H and Stamm M 2000 *Macromolecules* **33** 569
[55] Müller-Buschbaum P, Gutmann J S, Wolkenhauer M, Kraus J, Stamm M, Smilgies D and Petry W 2001 *Macromolecules* **34** 1396
[56] Daillant J and Bélorgey O 1992 *J. Chem. Phys.* **97** 5824
[57] Holý V and Baumbach T 1994 *Phys. Rev.* B **49** 10668
[58] Yoneda Y 1963 *Phys. Rev.* **131** 2010
[59] Cazabat A M 1990 *Liquids at Interfaces* (*Les Houches Session Series*) ed J Charvolin, J F Joanny and J Zinn-Justin (Amsterdam: Elsevier)
[60] Vrij A and Overbeek J T G 1968 *J. Am. Chem. Soc.* **90** 3074
[61] Brochard F and Daillant J 1990 *Can. J. Phys.* **68** 1084
[62] Brochard-Wyart F, Redon C and Sykes C 1992 *C. R. Acad. Sci.* II **19** 314
[63] Feng Y, Karim A, Weiss R A, Douglas J F and Han C C 1998 *Macromolecules* **31** 484
[64] Du B, Xie F, Wang Y, Yang Z and Tsui O K C 2002 *Langmuir* **18** 8510
[65] Henn G, Bucknall D G, Stamm M, Vanhoorne P and Jerome R 1996 *Macromolecules* **29** 4305
[66] Karapanagiotis I, Evans D F and Gerbrich W W 2002 *Colloids Surf.* A **207** 59
[67] Lorenz-Haas C, Müller-Buschbaum P, Kraus J, Bucknall D G and Stamm M 2002 *Appl. Phys.* A **74** S383
[68] Müller-Buschbaum P, Vanhoorne P, Scheumann V and Stamm M 1997 *Europhys. Lett.* **40** 655
[69] Müller-Buschbaum P and Stamm M 1998 *Physica* B **248** 229
[70] Müller-Buschbaum P, Gutmann J S and Stamm M 1999 *Phys. Chem. Chem. Phys.* **1** 3857
[71] Müller M, MacDowell L G, Müller-buschbaum P, Wunnicke O and Stamm M 2001 *J. Chem. Phys.* **115** 9960
[72] Reiter G 1992 *Phys. Rev. Lett.* **68** 75
[73] Reiter G 1993 *Langmuir* **9** 1344
[74] Seemann R, Jacobs K and Blossey R 2001 *J. Phys.: Condens. Matter* **13** 4915
[75] Seemann R, Herminghaus S and Jacobs K 2001 *J. Phys.: Condens. Matter* **13** 4925
[76] Seemann R, Herminghaus S and Jacobs K 2001 *Phys. Rev. Lett.* **86** 5534
[77] Stange T G, Mathew R, Evans D F and Hendrickson W A 1992 *Langmuir* **8** 920
[78] Xie R, Karim A, Douglas J F, Han C C and Weiss R A 1998 *Phys. Rev. Lett.* **81** 1251
[79] Yerushalmi-Rozen R, Klein J and Fetters L J 1994 *Science* **263** 793
[80] Yerushalmi-Rozen R and Klein J 1995 *Langmuir* **11** 2806
[81] Aubouy M 1997 *Phys. Rev.* E **56** 3370
[82] Rehse N, Wang C, Hund M, Geoghegan M, Magerle R and Krausch G 2001 *Eur. Phys. J.* E **4** 69
[83] Müller-Buschbaum P, Gutmann J S, Cubitt R and Stamm M 1999 *Colloid Polym. Sci.* **277** 1193
[84] Ade H, Winesett D A, Smith A P, Andres S, Stammler T, Heske C, Slep D, Rafailovich M H, Sokolov J and Stöhr J 1998 *Appl. Phys. Lett.* **73** 3775
[85] David M O, Reiter G, Sitthai T and Schultz J 1998 *Langmuir* **14** 5667
[86] Faldi A, Composto R J and Winey K I 1995 *Langmuir* **11** 4855
[87] Higgins A M and Jones R A L 2000 *Nature* **404** 476
[88] Higgins A M, Sferrazza M, Jones R A L, Jukes P C, Sharp J S, Dryden L E and Webster J 2002 *Eur. Phys. J.* E **8** 137
[89] Krausch G 1996 *Ber. Bunsenges. Phys. Chem.* **98** 446
[90] Lambooy P, Phelan K C, Haugg O and Krausch G 1996 *Phys. Rev. Lett.* **76** 1110
[91] Liu Y, Rafailovich M H, Sokolov J, Schwarz S A, Zhong X, Eisenberg A, Kramer E J, Sauer B B and Satija S 1994 *Phys. Rev. Lett.* **73** 440
[92] Pan Q, Winey K I, Hu H H and Composto R J 1997 *Langmuir* **13** 1758
[93] Pompe T, Fery A and Herminghaus S 1998 *Langmuir* **14** 2585
[94] Qu S, Clarke C J, Liu Y, Rafailovich M H, Sokolov J, Phelan K C and Krausch G 1997 *Macromolecules* **30** 3640
[95] Segalman R A and Grenn P F 1999 *Macromolecules* **32** 801
[96] Sferrazza M, Heppenstall-Butler M, Cubitt R, Bucknall D, Webster J and Jones R A L 1998 *Phys. Rev. Lett.* **81** 5173
[97] Wang C, Krausch G and Geoghegan M 2001 *Langmuir* **17** 6269
[98] Wunnicke O, Lorenz-Haas C, Müller-Buschbaum P, Leiner V and Stamm M 2002 *Appl. Phys.* A **74** S445
[99] Wunnicke O, Müller-Buschbaum P, Wolkenahuer M, Lorenz-Haas C, Cubitt R, Leiner V and Stamm M 2003 *Langmuir* **19** 8511
[100] Yuan C, Ouyang M and Koberstein J T 1999 *Macromolecules* **32** 2329

[101] Müller-Buschbaum P, O'Neil S A, Affrossman S and Stamm M 1998 *Macromolecules* **31** 5003
[102] Geoghegan M, Ermer H, Jüngst G, Krausch G and Brenn R 2000 *Phys. Rev.* E **62** 940
[103] Müller-Buschbaum P and Stamm M 2001 *Colloid Polym. Sci.* **279** 376
[104] Gutmann J S, Müller-Buschbaum P, Schubert D W, Stribeck N, Smilgies D and Stamm M 2000 *Physica* B **283** 40
[105] Walheim S, Böltau M, Mlynek J, Krausch G and Steiner U 1997 *Macromolecules* **30** 4995
[106] Walheim S, Ramstein M and Steiner U 1999 *Langmuir* **15** 4828
[107] Flebbe T, Dünweg B and Binder K 1996 *J. Physique* II **6** 667
[108] Binder K 1999 *Adv. Polym. Sci.* **138** 1
[109] Wagner A J and Yeomans J M 1998 *Phys. Rev. Lett.* **80** 1429
[110] Müller-Buschbaum P, Gutmann J S, Stamm M, Cubitt R, Cunis S, von Krosigk G, Gehrke R and Petry W 2000 *Physica* B **283** 53
[111] Müller-Buschbaum P, Cubitt R and Petry W 2002 *Appl. Phys.* A **74** S342
[112] Fasolka M J and Mayes A M 2001 *Annu. Rev. Mater. Res.* **31** 323
[113] Müller-Buschbaum P, Gutmann J S, Lorenz-Haas C, Mahltig B, Stamm M and Petry W 2001 *Macromolecules* **34** 7463
[114] Gießler K H, Rauch F and Stamm M 1994 *Europhys. Lett.* **27** 605
[115] Hamley I W, Hiscutt E L, Yang Y W and Booth C 1999 *J. Colloid Interface Sci.* **209** 255
[116] Morkved T L and Jaeger H M 1997 *Europhys. Lett.* **40** 643
[117] Müller-Buschbaum P, Gutmann J S, Cubitt R and Petry W 2004 *Physica* B **350** 207
[118] Müller-Buschbaum P 2003 *J. Phys.: Condens. Matter* **15** R1549
[119] Blossey R 2003 *Nat. Mater.* **2** 301
[120] Klapper H, Kobayashi M, Kobayashi T and Sato K 1991 *Organic Crystals* ed H C Freyhardt and C Müller (Berlin: Springer)
[121] Biscarini F, Samori R, Freco O and Zamboni R 1997 *Phys. Rev.* B **78** 2389
[122] Venables J A, Spiller G D and Hanbücken M 1984 *Rep. Prog. Phys.* **47** 399
[123] Brinkmann M, Biscarini F, Taliani C, Aiello I and Ghedini M 2000 *Phys. Rev.* B **61** R16339
[124] Brinkmann M, Graf S and Biscarini F 2002 *Phys. Rev.* B **66** 165430
[125] Weaire D and Rivier N 1984 *Contemp. Phys.* **25** 59
[126] Mulheran P A and Blackman J A 1996 *Phys. Rev.* B **54** 11681
[127] Sharma A and Ruckenstein E 1989 *J. Colloid Interface Sci.* **133** 358
[128] Sharma A and Ruckenstein E 1990 *J. Colloid Interface Sci.* **137** 433
[129] Binder K, Puri S and Frisch H L 1999 *Faraday Discuss.* **112** 103